Atmos. Meas. Tech., 9, 5227–5238, 2016
www.atmos-meas-tech.net/9/5227/2016/
doi:10.5194/amt-9-5227-2016

Atmospheric Measurement Techniques
Open Access
EGU

Quantification of uncertainties in OCO-2 measurements of XCO_2: simulations and linear error analysis

Brian Connor[1], Hartmut Bösch[2,6], James McDuffie[3], Tommy Taylor[4], Dejian Fu[3], Christian Frankenberg[5], Chris O'Dell[4], Vivienne H. Payne[3], Michael Gunson[3], Randy Pollock[3], Jonathan Hobbs[3], Fabiano Oyafuso[3], and Yibo Jiang[3]

[1]BC Scientific Consulting, Stony Brook, NY, USA
[2]EOS Group, Department of Physics and Astronomy, University of Leicester, Leicester, UK
[3]Jet Propulsion Laboratory, California Institute of Technology, Pasadena, CA, USA
[4]Cooperative Institute for Research in the Atmosphere, Fort Collins, CO, USA
[5]California Institute of Technology, Pasadena, CA, USA
[6]National Centre for Earth Observation NCEO, University of Leicester, Leicester, UK

Correspondence to: Brian Connor (bc.scientific.consulting@gmail.com)

Received: 13 April 2016 – Published in Atmos. Meas. Tech. Discuss.: 16 June 2016
Revised: 23 September 2016 – Accepted: 4 October 2016 – Published: 27 October 2016

Abstract. We present an analysis of uncertainties in global measurements of the column averaged dry-air mole fraction of CO_2 (XCO_2) by the NASA Orbiting Carbon Observatory-2 (OCO-2). The analysis is based on our best estimates for uncertainties in the OCO-2 operational algorithm and its inputs, and uses simulated spectra calculated for the actual flight and sounding geometry, with measured atmospheric analyses. The simulations are calculated for land nadir and ocean glint observations. We include errors in measurement, smoothing, interference, and forward model parameters. All types of error are combined to estimate the uncertainty in XCO_2 from single soundings, before any attempt at bias correction has been made. From these results we also estimate the "variable error" which differs between soundings, to infer the error in the difference of XCO_2 between any two soundings. The most important error sources are aerosol interference, spectroscopy, and instrument calibration. Aerosol is the largest source of variable error. Spectroscopy and calibration, although they are themselves fixed error sources, also produce important variable errors in XCO_2. Net variable errors are usually < 1 ppm over ocean and ∼ 0.5–2.0 ppm over land. The total error due to all sources is ∼ 1.5–3.5 ppm over land and ∼ 1.5–2.5 ppm over ocean.

1 Introduction

The Orbiting Carbon Observatory-2 (OCO-2) was launched on 2 July 2014 and has been making global measurements of CO_2 and O_2 spectral bands in reflected sunlight since early September 2014. Spectra are recorded in two CO_2 bands at 1.61 and 2.06 µm (WCO_2 and SCO_2, respectively), and the O_2 A-band at 0.76 µm with a resolving power between 17 000 and 20 000. These measurements are analyzed to provide estimates of the column-averaged dry-air mole fraction of CO_2, known as XCO_2. Details of the OCO-2 mission, measurement technique, and XCO_2 retrieval may be found in Crisp et al. (2008) and O'Dell et al. (2012). The instrument calibration is detailed in Rosenberg et al. (2016) and Lee et al. (2016). An overview of the results to be expected from OCO-2 was given by Bösch et al. (2011). These measurements are motivated primarily by the need to infer regional carbon fluxes, and to constrain global models of the carbon cycle. Characterizing the uncertainties in XCO_2 as measured, and in how these uncertainties vary in space and time, is critical for this purpose. Earlier studies of the error to be expected from such observations include Butz et al. (2009) and Jung et al. (2016). The present study is part of the ongoing effort at uncertainty quantification for the OCO-2 mission.

In this paper we assess the uncertainty in a single XCO_2 sounding by bottom-up analysis, using the best available

estimates of errors in the algorithm and its inputs ("error sources"), computing the contribution of each error source to uncertainty in XCO_2, and combining them to estimate net uncertainty. We further estimate the uncertainty in the difference of XCO_2 between any two soundings, by excluding the mean error produced by error sources that are constant in themselves. We compare XCO_2 uncertainties and their variability over land (nadir) and ocean (glint) for both June and December simulated data sets. Finally, we summarize the effect of all error sources globally, and identify those that are largest and most variable.

Our methodology is described in detail in Sects. 2 and 3 below. In overview, simulations of OCO-2 spectra were run with the CSU orbit simulator (O'Brien et al., 2009), retrievals were performed with the operational Level-2 (L2) code, and a linear error analysis was performed using a dedicated offline code. This study used simulations to allow full control of the calculations and their inputs. The use of simulations for this analysis should not significantly affect its overall conclusions or their applicability to OCO-2 operational measurements, since the simulations are calculated from "true states" drawn from a realistic atmosphere.

Simulated spectra were calculated for 3 days in June and 3 in December. Only nadir spectra were calculated over land, and only glint spectra over ocean. Calculations were done for a single footprint (as opposed to eight footprints for the flight data), with the sounding frequency set at 1 Hz (as compared to 3 Hz in operation). The resulting reduction in data volume (factor of 24) was done purely for convenience and should not affect conclusions from this study. After cloud screening using the oxygen A-band preprocessor (ABP) (Taylor et al., 2016), the operational L2 code was run on the simulations, and the results were screened for convergence. A second screen was performed to minimize the occurrence of outliers, by restricting the accepted range of some sounding and retrieved parameters. More than 20 000 soundings passed these screens, and those were run with the L2 code a second time, using an extended state vector including a set of interfering aerosols. The interfering aerosols are tightly constrained to very small values in this step, but are included to force the L2 code to calculate their Jacobians. The Jacobian matrix, $\mathbf{K}$, for the extended state vector was saved for later analysis. (The Jacobian matrix contains the first-order partial derivatives of the forward model with respect to the state vector elements, i.e., $\mathbf{K} = \mathrm{d}F(\boldsymbol{x})/\mathrm{d}\boldsymbol{x}$.) In addition, Jacobians were evaluated for a range of forward model errors, and were also saved.

Linear error analysis (Rodgers, 2000; Rodgers and Connor, 2003) was performed on the extended L2 output, using an offline code developed for the purpose (Connor et al., 2008). We calculate actual uncertainties using estimates of true error in the measured spectrum, the variability of the atmospheric ensemble, and forward model errors.

These calculations are intended to apply to a comparison of L2 results to the true atmospheric values, without applying a "bias correction" (Wunch et al., 2011) to the L2 results.

The paper is organized as follows. In Sect. 2 we briefly discuss the L2 retrieval algorithm and then present details of the error analysis methodology. This is followed by an enumeration and discussion of the error sources to be considered in Sect. 3. Section 4 contains the results of the linear error analysis. Section 5 is a discussion of the results, and Sect. 6 identifies needs for future research.

2 Background and methodology

The OCO-2 level 2 full physics retrieval algorithm ("L2"), consists of a forward model and inverse method, described in full detail in JPL (2015). The forward model is a radiative transfer model of the atmosphere coupled to a model of the solar spectrum to calculate the monochromatic spectrum at the top of the atmosphere, which is then convolved with the response function as measured for the OCO-2 instrument. The inverse method is a maximum a posteriori likelihood method of a type which has been widely used in the community (Rodgers, 2000; Rodgers and Connor, 2003; Connor et al., 2008, O'Dell et al., 2012). For comparison, the retrieval algorithm for the spectrally similar measurements by the GOSAT satellite is described in Yoshida et al. (2011). Uncertainty in the OCO-2 measurements of XCO_2 has been assessed using an offline error analysis code developed for the purpose (Connor et al., 2008).

2.1 Formulation

The error analysis algorithm performs a linear analysis using Jacobians calculated by the operational OCO-2 forward model. This section closely follows the discussion in Connor et al. (2008).

As defined in JPL (2015), $\mathbf{S}_\mathrm{a}$ is the a priori covariance matrix, $\mathbf{S}_\varepsilon$ is the measurement error covariance matrix, and $\mathbf{K}$ is the weighting function (Jacobian) matrix. The offline calculations are more detailed and more realistic than error estimates performed operationally. For example, if forward model errors are included in the $\mathbf{S}_\varepsilon$ matrix used operationally, the retrieved state may be systematically biased by the a priori state. Thus we evaluate the effect of forward model errors offline. Further, evaluation of the smoothing and interference errors strictly requires the covariance of the ensemble of true states, $\mathbf{S}_\mathrm{c}$, which is not necessarily equal to the a priori covariance $\mathbf{S}_\mathrm{a}$ (Rodgers and Connor, 2003). The authors' experience with other remote sensing retrievals suggests that the a priori constraint, embodied in $\mathbf{S}_\mathrm{a}$, should be as uniform as practical over all soundings, to avoid introducing an additional source of variability. However, the covariance of true states, $\mathbf{S}_\mathrm{c}$, varies with latitude, longitude, and season. Estimates of $\mathbf{S}_\mathrm{c}$ are readily included in the offline error estimates (see for example Sect. 3.3.1.)

Equations (1)–(6) follow the definitions of Rodgers (2000) and Rodgers and Connor (2003). Given $\mathbf{K}$, $\mathbf{S}_\varepsilon$, and $\mathbf{S}_\mathrm{a}$, we first characterize the operational retrieval by calculating the gain function $\mathbf{G}_y$ and the averaging kernel matrix $\mathbf{A}$:

$$\mathbf{G}_y = \left(\mathbf{K}^T\mathbf{S}_\varepsilon^{-1}\mathbf{K} + \mathbf{S}_\mathrm{a}^{-1}\right)^{-1}\mathbf{K}^T\mathbf{S}_\varepsilon^{-1} \quad (1)$$

and

$$\mathbf{A} = \mathbf{G}_y\mathbf{K}. \quad (2)$$

We then specify a list of estimated errors to include in the calculation, and where possible the correlation between errors. We will refer to these as error sources. Next we assemble these into an ensemble covariance $\mathbf{S}_\mathrm{c}$ (for elements in the state vector) and a forward model parameter covariance $\mathbf{S}_b$ (for elements not included in the state vector). Finally, we calculate the Jacobian matrix with respect to the forward model parameters, denoted $\mathbf{K}_b$.

For each error in the list, we calculate the resulting covariance of the retrieved state vector, as follows. For measurement error,

$$\hat{\mathbf{S}}_\mathrm{m} = \mathbf{G}_y\mathbf{S}_\delta\mathbf{G}_y^T, \quad (3)$$

where $\mathbf{S}_\delta$ may be equal to $\mathbf{S}_\varepsilon$, or an alternative estimate of the actual measurement covariance. In the work presented here, $\mathbf{S}_\delta = \mathbf{S}_\varepsilon$.

For forward model error,

$$\hat{\mathbf{S}}_\mathrm{f} = \mathbf{G}_y\mathbf{K}_b\mathbf{S}_b\mathbf{K}_b^T\mathbf{G}_y^T. \quad (4)$$

For smoothing error,

$$\hat{\mathbf{S}}_\mathrm{s} = (\mathbf{A}-\mathbf{I})\mathbf{S}_\mathrm{c}(\mathbf{A}-\mathbf{I})^T, \quad (5)$$

where $\mathbf{I}$ is the identity matrix.

For interference error, which refers to error in CO_2 caused by non-CO_2 components of the state vector,

$$\hat{\mathbf{S}}_i = \mathbf{A}_{ue}\mathbf{S}_\mathrm{ec}\mathbf{A}_{ue}^T, \quad (6)$$

where $\mathbf{S}_\mathrm{ec}$ is the ensemble covariance for the non CO_2 elements $\boldsymbol{e}$, and $\mathbf{A}_{ue}$ is the off-diagonal block of the averaging kernel matrix that relates $\boldsymbol{e}$ to the CO_2 profile $\boldsymbol{u}$.

Finally, the total covariance is

$$\hat{\mathbf{S}} = \hat{\mathbf{S}}_\mathrm{m} + \hat{\mathbf{S}}_\mathrm{s} + \hat{\mathbf{S}}_i + \hat{\mathbf{S}}_\mathrm{f}, \quad (7)$$

and the resulting variance of XCO_2 is $\sigma^2_{\mathrm{XCO2}} = \boldsymbol{h}^T\hat{\mathbf{S}}\boldsymbol{h}$, where $\boldsymbol{h} = \partial X_{\mathrm{CO2}}/\partial\boldsymbol{x}$ represents the pressure weighting function. Alternatively, one may calculate the variance in XCO_2 due to a given error source, r, as $\sigma_r^2 = \boldsymbol{h}^T\hat{\mathbf{S}}_r\,\boldsymbol{h}$ and sum the variances for all r.

The discussion of the preceding paragraph makes two assumptions – one, that the retrieval is approximately linear within the region bounded by its uncertainty, and two, that the error sources considered are themselves uncorrelated. Whenever error sources are correlated, the correlations must be included in, e.g., Eqs. (4) or (6), and the net effect on XCO_2 calculated for the combined correlated sources.

2.2 Treatment of fixed error sources

Many of the error sources we will consider do not vary randomly, and some do not vary at all. Spectroscopic errors belong to the class of error sources that are truly fixed. Unfortunately, due to the varying amount of information in each measured spectrum relative to the a priori constraint, embodied in changes in the gain function, $\mathbf{G}_y$, the resulting errors in retrieved XCO_2 are not fixed. We will treat such errors as follows.

We note that the gain function, $\mathbf{G}_y$, represents the sensitivity of the state vector to the measured radiances. Combining that with the definition of $\mathbf{K}_b$, and considering for the moment a single scalar parameter, the error caused by parameter b is

$$\hat{\boldsymbol{x}} - x = \boldsymbol{h}^T\mathbf{G}_y\mathbf{K}_b\mathrm{d}b, \quad (8)$$

where $\hat{\boldsymbol{x}} - x$ is the retrieved XCO_2 minus the true XCO_2, or we may write

$$\hat{\boldsymbol{x}} - x = \left(\boldsymbol{h}^T\mathbf{G}_y\mathbf{K}_b\mathrm{d}b^2\mathbf{K}_b^T\mathbf{G}_y^T\boldsymbol{h}\right)^{1/2}. \quad (9)$$

Replacing $\mathrm{d}b^2$ with its matrix equivalent $\mathbf{S}_b$, then for an ensemble of retrievals,

$$\sigma_x = \mathrm{rms}(\hat{x} - x) = \mathrm{rms}\left[\left(\boldsymbol{h}^T\mathbf{G}_y\mathbf{K}_b\mathbf{S}_b\mathbf{K}_b^T\mathbf{G}_y^T\boldsymbol{h}\right)^{1/2}\right], \quad (10)$$

where rms denotes the root mean square error. Therefore, if $\mathrm{d}b$ is a constant, the error $\hat{\boldsymbol{x}} - x$ caused by it will vary about a mean value given by σ_x. While the true error in parameter b is an unknown constant, we assume that error is equal to the uncertainty in b.

2.3 Variable error

Sources and sinks of CO_2 and the circulation of the atmosphere produce temporal and spatial gradients in the XCO_2 field, which are quantitatively predicted by carbon cycle models. Measuring these gradients is a strong test of such models. Thus, errors which vary from sounding to sounding limit the efficacy of the OCO-2 measurements in constraining carbon cycle models. On the other hand, an error that is constant, or at least has a well-defined mean value, can be subtracted from all soundings with minimal or no effect on gradients of XCO_2. Therefore, we have attempted to distinguish the uncertainty that differs between soundings; i.e., it applies to a difference in two soundings, from the total accuracy.

We will refer to this differential uncertainty as "variable error". By its nature, variable error has both random components and those which are systematic in the sense that they depend on conditions such as solar zenith angle, atmospheric temperature, pressure, and aerosol, and surface properties. In

other words, the concept of variable error applies to the difference between any two soundings, but its magnitude will depend on the difference in conditions between them.

Our quantitative estimate of variable error is a composite error calculated from a selection taken from all error sources described above. Variable error will be calculated from all error sources, but will exclude the mean error produced by fixed error sources as discussed in Sect. 2.2. Then a first approximation to the predicted error in the difference of XCO_2 between two soundings will simply be the variable error multiplied by $\sqrt{2}$, assuming remaining errors are uncorrelated in space or time. This should be equivalent to estimating the net uncertainty in each sounding, and assuming a simple bias correction relative to validation observations has been performed.

3 Error types

We will consider four types of error: measurement, smoothing, interference, and forward model.

3.1 Measurement error

The first and most obvious error is random noise in the measured spectrum. This is calculated based on the operational noise model (JPL, 2015), and its direct effect on XCO_2 is calculated, and tabulated as "measurement error."

However, it is observed that spectral residuals do not decrease with averaging as would be expected for pure random noise, but instead have a systematic structure. Because of this it was decided to derive empirical orthogonal functions (EOFs) representing this systematic structure, and to retrieve scale factors for these functions at every sounding (see Sect. 3.3.2.6 of JPL, 2015). Uncertainties in this process are to be addressed as interference error, below.

3.2 Smoothing error

This represents error due to the a priori constraint of the state vector. As suggested by Rodgers and Connor (2003), we have separated this into two components. The first, smoothing by the true CO_2 profile, which we simply refer to as "smoothing", is discussed here. The second component is error introduced into XCO_2 by the non-CO_2 elements of the state vector, which we call "interference", discussed in the following section.

The error due to the true atmospheric CO_2 profile would be best estimated by using the covariance of the ensemble of true states, $\mathbf{S}_c$. Exactly which states to include in the ensemble is not well defined. We have chosen to use the a priori covariance $\mathbf{S}_a$, which is intended to represent the variability of CO_2 globally throughout the year. We will systematically overestimate the smoothing error as a result. However, the smoothing error is always small, as we will see, and the use of $\mathbf{S}_a$ is fundamentally conservative.

3.3 Interference error

3.3.1 Aerosol and cloud

We apply the Modern Era Retrospective analysis for Research and Applications (MERRA) aerosol reanalysis climatology for daytime (local time 10:00, 13:00, and 16:00) in June and December, to represent the aerosol-related variability in the OCO-2 spectral measurements (Rienecker et al., 2011). The MERRA aerosol data are the basis for the OCO-2 forward model's aerosol types, as described in detail in JPL (2015, pages 28–31). MERRA aerosol data consisting of five composite types, namely dust (DU), sea salt (SS), sulfate (SU), black carbon (BC), and organic carbon (OC), have nearly zero bias and a correlation coefficient of ~ 0.9 with respect to the collocated aerosol optical depth (AOD) measurements from AErosol RObotic NETwork (AERONET), Multi-angle Imaging SpectroRadiometer (MISR), and Ozone Monitoring Instrument (OMI) (Buchard et al., 2015). At each sounding location, the two composite types most common at that location are included in the state vector for the operational retrieval, along with liquid water and ice cloud, and are retrieved by the L2 algorithm. For the analysis presented here we take into account the variability of all five type of aerosols, including those not retrieved, as described next.

The L2 calculations for linear error analysis are performed at each sounding with the operational state vector and a priori uncertainties, augmented as follows. Ten additional aerosol quantities are added to the state vector, namely the AOD for each of the five composite MERRA aerosols, integrated over two layers. Using the relative pressure scale σ, defined as the fraction of surface pressure, the lower layer is at $\sigma = 0.95$ with width 0.05, while the upper layer is at $\sigma = 0.5$ with width 0.2. The a priori amount and uncertainty for each of these 10 aerosol quantities is set equal to a small positive number, nonzero to avoid singularity, but small enough to have negligible effect on the algorithm. The L2 algorithm then calculates the Jacobians for each of these 10 interfering aerosol species.

Subsequently, the linear error analysis combines the Jacobians for all of the aerosol and cloud quantities (liquid water, ice, the two types retrieved, and the 10 additional interfering aerosols) with estimates of the ensemble variability of their total atmospheric AOD, to calculate the resulting error in XCO_2. For this step, we have created a database of the standard deviation of each of the five MERRA composite types, in two layers defined as the surface to 750 and 750 hPa to top of atmosphere, on a $2.5^\circ \times 2.5^\circ$ lat/long grid, for each month. For each sounding location, our error analysis algorithm looks up the standard deviation at the nearest grid point for all 10 aerosols, and uses that as the estimated ensemble variability. For liquid water and ice cloud, we assume the ensemble variance equals the a priori variance. The a priori uncertainty of liquid water and ice (approximately a factor 6,

1σ) was deliberately set large enough to minimize its effect on retrieved XCO_2.

The two retrieved aerosol types are counted twice by this procedure, once in the operational state vector and again in the part of the state vector as augmented for the error analysis. To avoid an error due to "double counting", we set the ensemble variance for the aerosols in the operational state vector to very small values, ensuring they produce negligible error in retrieved XCO_2.

3.3.2 Empirical orthogonal functions (EOFs)

Interference errors due to the scale factors applied to the operational EOFs are calculated as part of the error analysis by including the actual EOF scale factors in the state vector. The results show negligible effects on XCO_2 uncertainties and degrees of freedom due to these scale factors.

3.3.3 Other interference errors

Other non-CO_2 components of the state vector include surface pressure, water vapor column, an offset to the a priori temperature, a linear dispersion coefficient for each spectral band (defining the separation in wavelength between adjacent pixels), albedo, and the linear change in albedo across each spectral band. Land (nadir) observations also include a coefficient of fluorescence, and ocean (glint) observations include wind speed. These have all been included in the error analysis.

For all of these components, an effort has been made to include an estimate of global variability as the a priori uncertainty, and this has been used as the estimated ensemble variability in the error analysis. The net effect of these uncertainties is fairly small compared to aerosols and forward model errors, so refining this ensemble estimate has not been a high priority, but may be considered later.

3.4 Forward model error

Forward model errors that have been evaluated in this analysis include those due to a variety of spectroscopic and calibration parameters.

Table 1 shows the estimated uncertainties in spectroscopic parameters used in the L2 algorithm. The parameters listed are those required for the spectroscopic line shape models used within the OCO-2 v7 L2 algorithm. For CO_2 this is a speed-dependent Voigt line shape with tridiagonal line mixing and for O_2, this is a Voigt line shape with first-order line mixing, with a contribution from collision-induced absorption (CIA). The relevant references, describing these parameters and the uncertainty estimates, are given in the table.

The majority of the uncertainties listed in Table 1 are based on published values. The notable exceptions are speed dependence in the CO_2 bands and line mixing in the O_2 A-band. Fairly large uncertainties have been estimated for these by L. Brown at the Jet Propulsion Laboratory (JPL) (L. Brown, personal communication, 2014).

Table 1. Uncertainties in spectroscopic parameters used in the L2 algorithm.

	Band	Uncertainty	Reference
Line strength	SCO_2	0.40 %	Joly et al. (2009)
	WCO_2	0.30 %	Devi et al. (2007, 2016)
	O_2-A	0.40 %	Long et al. (2010)
Air broaden.	SCO_2	0.15 %	Joly et al. (2009)
	WCO_2	0.10 %	Devi et al. (2007)
	O_2-A	0.20 %	Robichaud et al. (2008)
T-width	SCO_2	0.45 %	Joly et al. (2009)
	WCO_2	0.60 %	Devi et al. (2007)
	O_2-A	1.25 %	Drouin et al. (2016)
CIA	O_2-A	0.1[a]	Long et al. (2012)
H_2O broaden.	SCO_2	3 %	Sung et al. (2009)
	WCO_2	3 %	Sung et al. (2009)
Pressure shift	SCO_2	2.60 %	Joly et al. (2009)
	WCO_2	1.50 %	Devi et al. (2007)
	O_2-A	2 %	Robichaud et al. (2008)
Line mixing	SCO_2	10 %	Benner et al. (2011)
	WCO_2	10 %	Benner et al. (2011)
	O_2-A	10 %	estimate[b]
Speed dep.	SCO_2	10 %	estimate[b]
	WCO_2	10 %	estimate[b]

[a] 10^{-7} cm^{-1} $amagat^{-2}$;
[b] L. Brown, personal communication, 2014.

It is also worth noting that the exponent of the temperature dependence of the pressure broadened line widths in the O_2-A band has been measured recently by Droiun et al. (2015). The absolute value of this parameter differs by ~ 8 % from the previously published value (Brown and Plymate, 2000), which was used in the OCO-2 data processing up to and including v7. The newer, Drouin et al value will change the derived XCO_2 values by ~ 1 ppm.

A discrepancy between recent measurements of the line strength in the WCO2 band is also of note. The values used by the OCO-2 algorithm are based on Devi et al. (2007, 2016). Values from Polyansky et al. (2015) differ from those in Devi et al. (2016) by ~ 1.2 %.

Spectroscopic uncertainties in interfering gas species are not a significant source of error in retrieved XCO_2. The strongest interferent, by far, is H_2O, and its largest uncertainties are in its pressure broadening. Earlier tests of the L2 algorithm (not part of the present analysis) evaluated H_2O line parameters with broadening coefficients 20 % different from reference values, and found mean XCO_2 changes of < 0.01 ppm, with apparently random distribution. Therefore we have not included spectroscopic uncertainties in any interfering species in Table 1, and will not discuss them further.

Table 2. Uncertainties in calibration parameters used in the L2 algorithm.

	Uncertainties	Correlations
ILS		
O_2-A	0.25 %	0.7 to SCO_2 and WCO_2
WCO_2	0.25 %	0.8 to SCO_2
SCO_2	0.40 %	
Radiometric gain		
O_2-A	1.10 %	0.5 to WCO_2 and SCO_2
WCO_2	1.50 %	
SCO_2	1.60 %	
Polarization angle		
O_2-A	0.5°	
WCO_2	0.5°	
SCO_2	0.5°	

Uncertainties in the calibration parameters are shown in Table 2. These are based on pre-flight laboratory calibration of the instrument at the Jet Propulsion Laboratory. The parameters are defined as follows. The instrument line shape (ILS) in each band is assumed to have a single uncertainty, in its width. Its shape as measured in the laboratory before launch is assumed to be correct. Radiometric gain is the factor applied to the measured voltages to convert them to absolute physical units. Finally, OCO-2 is only sensitive to one polarization of the incoming radiation, whose angle of orientation is the "polarization angle".

In applying the uncertainties in polarization angle, we note that the observed spectrum **S** may be written in terms of the Stokes parameters **I**, **Q**, **U**, and **V**, and Mueller matrix coefficients m_I, m_Q, m_U, and m_V:

$$\mathbf{S} = m\_\mathrm{I} \times \mathbf{I} + m\_\mathrm{Q} \times \mathbf{Q} + m\_\mathrm{U} \times \mathbf{U} + m\_\mathrm{V} \times \mathbf{V}. \quad (11)$$

Uncertainties in the Mueller matrix coefficients were calculated as follows. First,

$$m\_\mathrm{I} = 0.5$$
$$m\_\mathrm{Q} = 0.5 \times \cos(2 \times \phi_{\mathrm{pol}})$$
$$m\_\mathrm{U} = 0.5 \times \sin(2 \times \phi_{\mathrm{pol}})$$
$$m\_\mathrm{V} = 0.$$

The uncertainty in the polarization angle ϕ_{pol} is ±0.5° (Table 2, 1σ) for all three bands, m_Q and m_U are derived from the same measurement, so have correlation = 1, and the three bands should be independent. From the above, a 3×3 covariance matrix can readily be calculated, which applies to all three bands (uncertainty in m_I is assumed to be nonzero, but very small, to avoid singularity). Note that **V**, the circular component of polarizaton, is completely ignored in the L2 algorithm as there are very few natural sources.

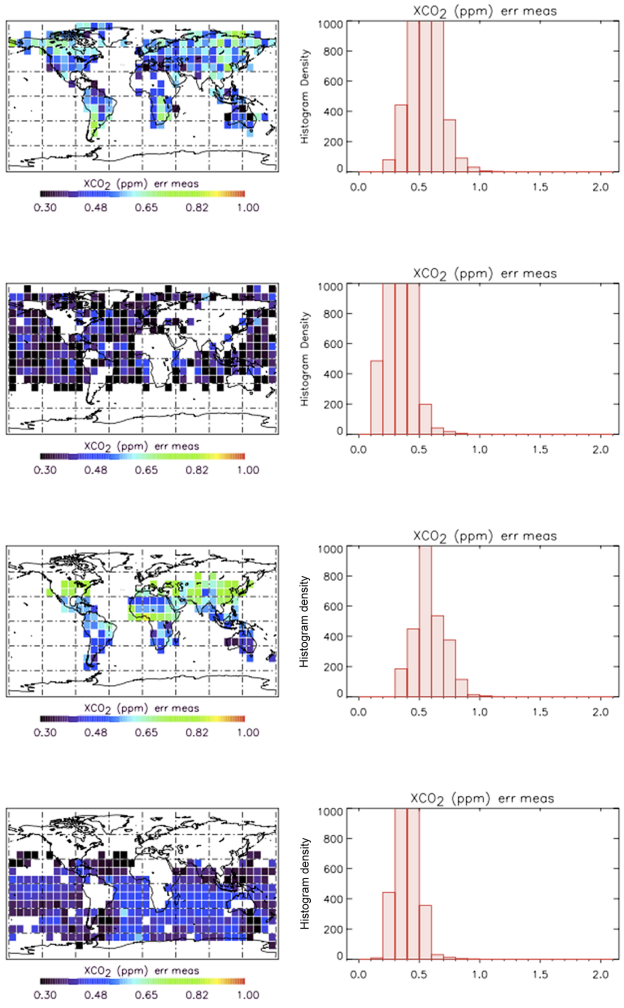

Figure 1. Measurement error. Top: June, land; second row: June, ocean; third row: Dec., land; bottom: Dec., ocean.

4 Results

Figures 1–6 and Tables 3 and 4, below, display the summary of results for the offline error analysis. The data are gridded into $10° \times 10°$ bins, and only bins with a minimum of three soundings are displayed. An overall observation is that there is some spatial seasonal dependence in all of the error types due to the shifting subsolar point of the sun from summer to winter, which drives signal- and air-mass-related errors.

Figure 1 shows measurement error due to random noise in the measured spectra. It is typically ∼0.5 ppm for a single sounding, and is expected to decrease with averaging approximately as expected for random error, i.e., in proportion to $\sqrt{N}$, for N = the number of soundings in the average. The error is smaller and more uniform for ocean than land, presumably due to the increased signal-to-noise ratio in glint viewing mode.

Forward model error, divided into spectroscopic and instrument error, is shown in Figs. 2 and 3, respectively. Spec-

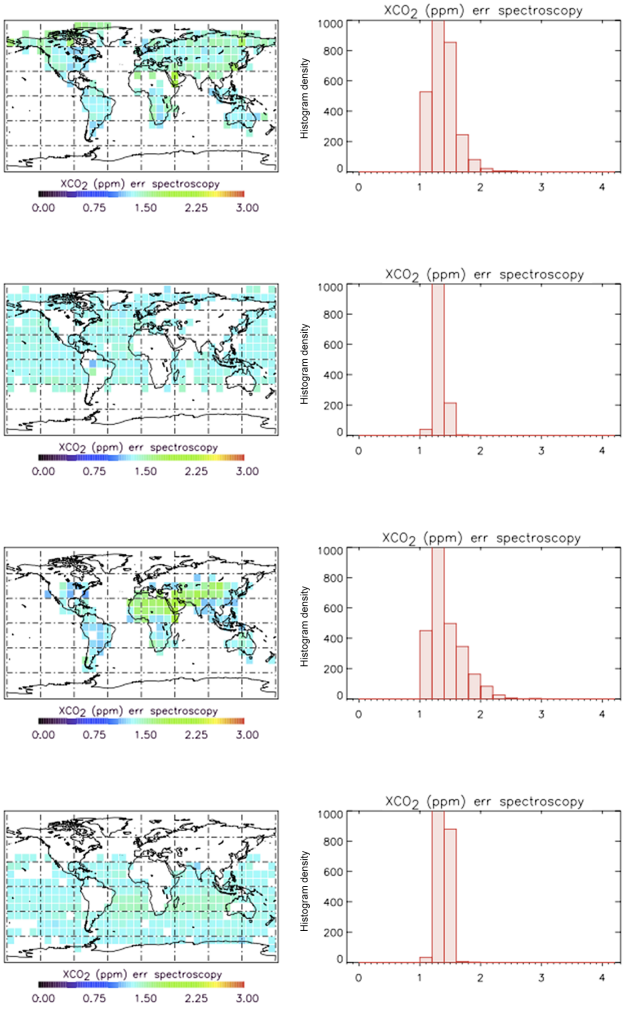

Figure 2. Error due to spectroscopy. Top: June, land; second row: June, ocean; third row: Dec., land; bottom: Dec., ocean.

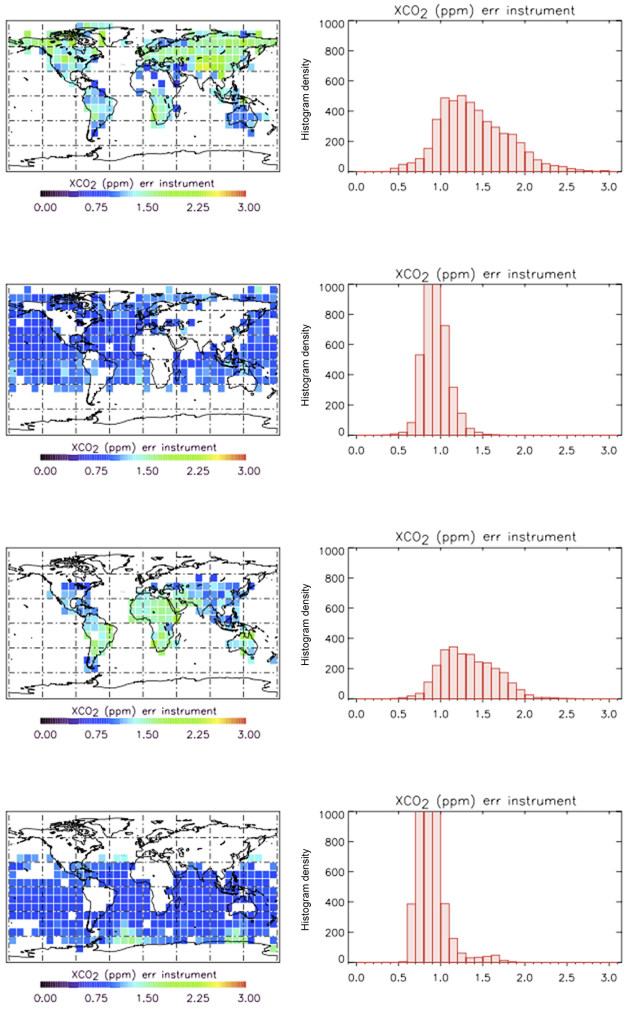

Figure 3. Instrument error. Top: June, land; second row: June, ocean; third row: Dec., land; bottom: Dec., ocean.

troscopic and instrument error make roughly equal contributions to forward model error. Spectroscopic error in ocean glint observations shows little variation, and is ~ 1.3 ppm. For land nadir it is more variable, typically 1–2 ppm. The most important spectroscopic error is due to uncertainty in the WCO_2 band strength (Tables 3 and 4). Instrument error is somewhat more variable, especially over land. It is ~ 1 ppm in ocean glint and ~ 0.5–2.5 in land nadir. The most important instrument error is due to uncertainty in the instrument line shape (ILS).

Maps of aerosol error are shown in Fig. 4a, and for comparison, the monthly mean aerosol optical depth from MERRA is shown in Fig. 4b and its standard deviation in Fig. 4c. The sensitivity of XCO_2 to interference error caused by the various aerosol types is shown in the Supplement published with this paper.

In most places, aerosol errors are surprisingly small, typically ~ 0.5 ppm. However there are regions where they are systematically larger, ~ 2.0–2.5 ppm. These regions include east Asia, which has highly variable aerosol loading, and the tropical North Atlantic, due to dust (not shown), presumably from north Africa. There are also systematically large errors over the Arctic Ocean. We believe these occur because of high sensitivity of the algorithm to small spectral errors at high solar zenith angle.

Variable error is shown in Fig. 5. Comparison to Figs. 3 and 4 shows that variable error over land is dominated by instrument error (due to instrument line shape), but also by aerosol error over ocean. It is typically ~ 0.5–2.0 ppm in land nadir, and mostly < 1 ppm in ocean glint, but as for aerosol, it is 2.0–2.5 ppm in glint in some regions.

Total error from all sources is shown in Fig. 6. It is ~ 1.5–3.5 ppm over land and ~ 1.5–2.5 ppm over ocean.

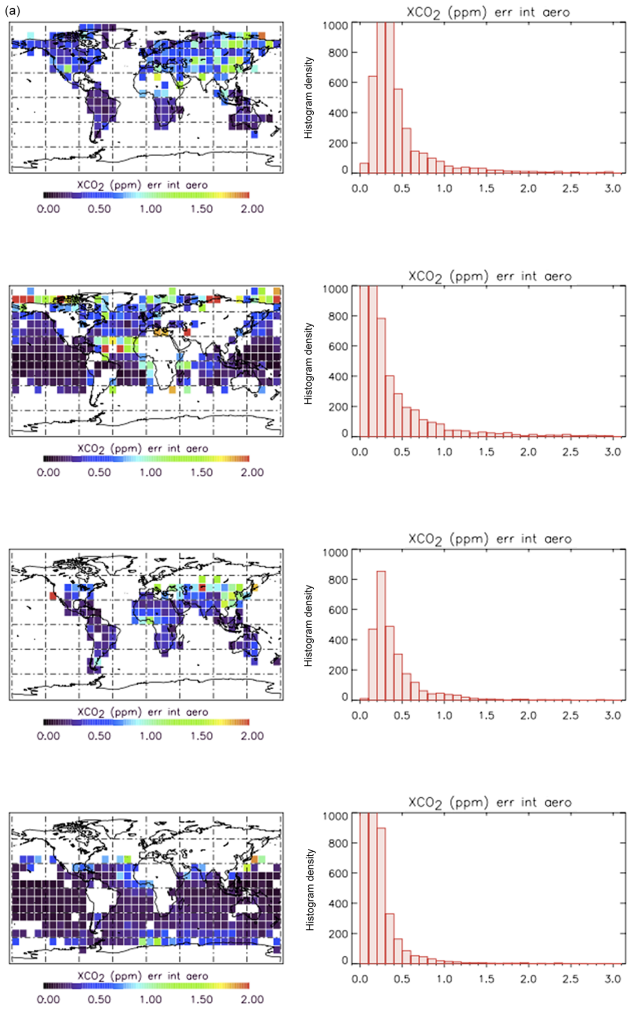

Figure 4. (a) Aerosol error. Top: June, land; second row: June, ocean; third row: Dec., land; bottom: Dec., ocean.

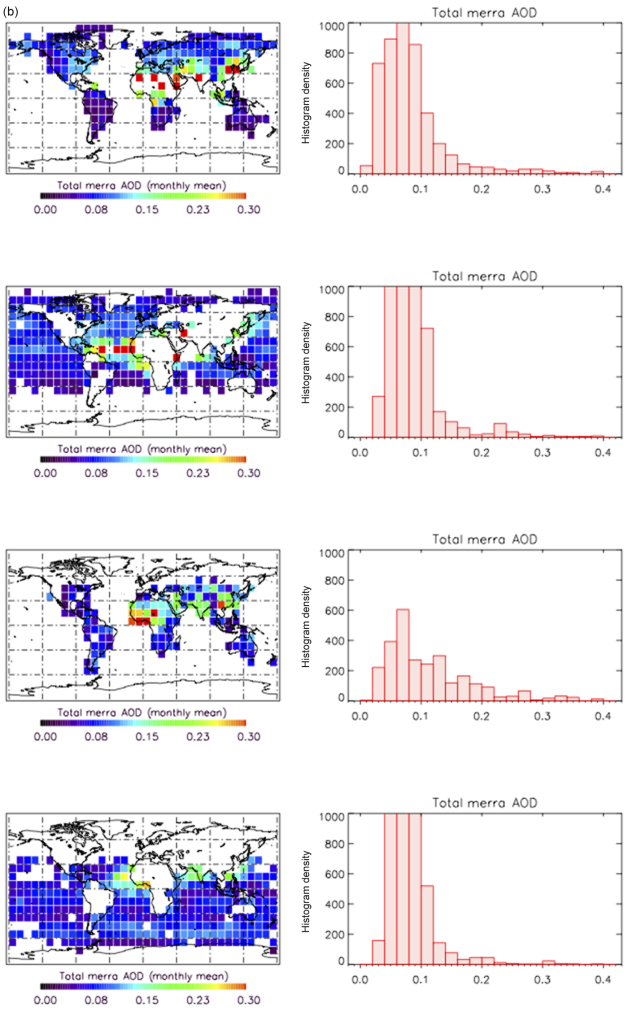

Figure 4. (b) Monthly mean aerosol optical depth (AOD) from MERRA. Top: June, land; second row: June, ocean; third row: Dec., land; bottom: Dec., ocean.

5 Discussion

Inspection of the global mean and standard deviations in Tables 3 and 4 gives rise to some interesting observations. In general, the fixed, or approximately fixed, error sources (spectroscopy and instrument calibration) cause mean errors much larger than their standard deviations. This implies that whatever the true value of the error in the relevant forward model parameter, most of its effect can in principle be removed by simple bias correction based on validation measurements. However, the remaining, variable error, caused by the fixed error source, is of critical importance. The error in the difference in XCO_2 between two soundings is better characterized by the variability of that parameter's effect than by its mean; i.e the mean effect is the same for both soundings and is removed by taking their difference. This is the rationale for our definition and use of variable error, as discussed in Sect. 3. It is also worth noting that both the mean and standard deviation of errors due to fixed sources are larger for land nadir than for ocean glint soundings.

As noted above, spectroscopic error varies little over the ocean, and modestly over land. The main sources of this behavior can be traced to WCO_2 and O_2 line strength, which are the largest error sources but are fairly constant in both regimes, and SCO_2 and O_2 line mixing, which have highly variable effects over land, and little variation over ocean.

Three components of instrument error were analyzed. Error due to uncertainty in the polarization angle ϕ_{pol} is negligible, < 0.01 ppm (not shown elsewhere). Uncertainty in instrument gain is a significant but fairly small source of XCO_2 error, averaging 0.2–0.3 ppm. The behavior of the instrument error is dominated by the ILS; uncertainties in XCO_2 due to the ILS are the largest single error source over land, with variability second only to aerosol ($\sim 1.4 \pm 0.4$ ppm). Preflight measurements of the ILS were done to high accuracy

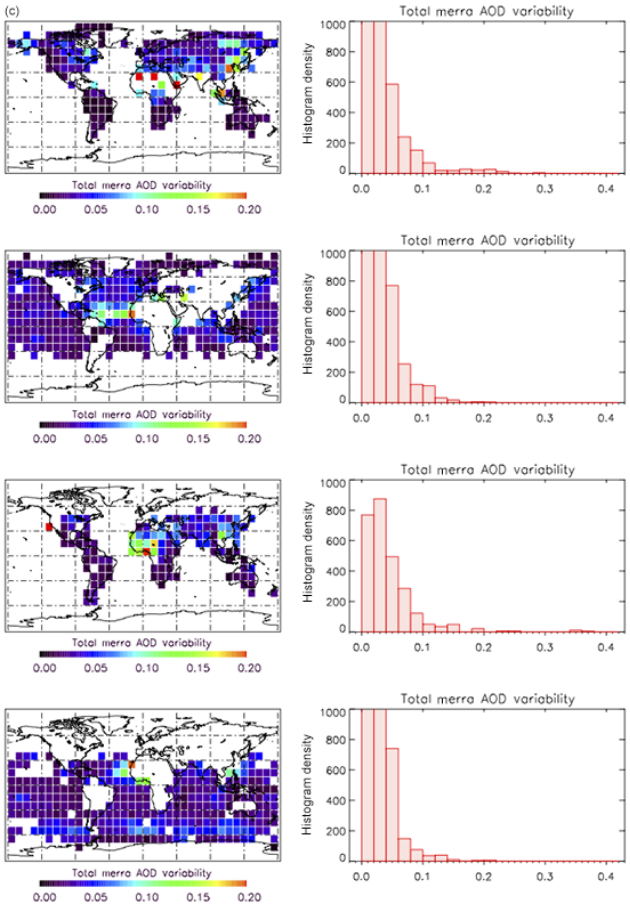

Figure 4. (c) Monthly standard deviation of aerosol optical depth (AOD) from MERRA. Top: June, land; second row: June, ocean; third row: Dec. land; bottom: Dec., ocean.

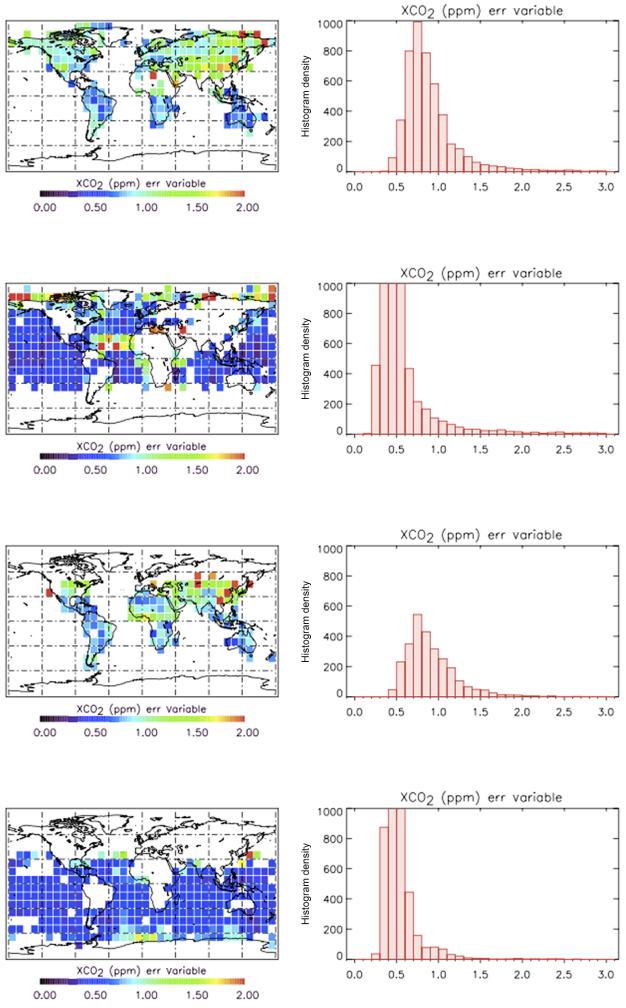

Figure 5. Variable error. Top: June, land; second row: June, ocean; third row: Dec. land; bottom: Dec., ocean.

(Table 2), but the sensitivity of XCO_2 to the ILS is high. Error due to the ILS is larger and much more variable over land than over ocean.

Uncertainty due to smoothing error is fairly small. It is typically ≤ 0.2 ppm. The full results (not shown) indicate it is rarely, if ever, larger than 0.4 ppm. The magnitude of smoothing error was deliberately minimized by choice of a loose a priori constraint on the CO_2 profile in the L2 algorithm. It is likely to vary systematically with local conditions, since it arises in the difference between the actual and a priori CO_2 profile shapes.

Tables 3 and 4 also emphasize that the dominant variable error is due to aerosol. Although the absolute size of the aerosol error is fairly small, it varies widely from place to place, with a standard deviation up to 195 % of its mean value (the coefficients of variation are 134, 109, 195, and 132 % for June nadir – land, Dec. nadir – land, June glint – water, and Dec. glint – water, respectively). Furthermore, it will depend on the actual atmospheric aerosol distribution, which will vary in a complex fashion with space and time. Correlation of the aerosol distribution is likely to be a major source of correlation in XCO_2 error, which will be difficult to characterize quantitatively.

6 Recommendations for further research

We envisage a continual ongoing analysis to quantify uncertainties in the OCO-2 measurements. We believe such quantification is critical for using the data to constrain the geophysical carbon cycle. Linear error analysis as presented here will be a key part of that effort, and it is important to replicate the analysis when future versions of the L2 algorithm are released and mission data are reprocessed. The error analysis should be extended to further examine errors produced by the algorithm itself. This would include studying the effect of errors in algorithm inputs such as the a priori state vector. A more general subject for study is nonlinearity of the forward and inverse models. Both of these areas are foci of active research. In the particular case of nonlinearity, linear error analysis can be supplemented with Monte Carlo studies.

Table 3. Global mean errors in XCO_2 and standard deviations for land nadir observations. The coefficient of variation (relative standard deviation) is also shown.

	June		December	
Measurement	0.55 ± 0.12	22 %	0.58 ± 0.12	21 %
SCO_2 line strength	0.23 ± 0.15	65 %	0.28 ± 0.18	64 %
WCO_2 line strength	0.94 ± 0.16	17 %	0.92 ± 0.21	23 %
O_2 line strength	0.55 ± 0.14	25 %	0.57 ± 0.09	16 %
O_2 line width	0.27 ± 0.08	30 %	0.28 ± 0.05	18 %
O_2 width T dependence	0.11 ± 0.06	55 %	0.19 ± 0.09	47 %
Line mixing SCO_2	0.40 ± 0.26	65 %	0.52 ± 0.36	69 %
Line mixing O_2	0.21 ± 0.17	81 %	0.22 ± 0.17	77 %
Speed dependence WCO_2	0.32 ± 0.06	19 %	0.34 ± 0.10	29 %
Total spectroscopy	1.35 ± 0.17	13 %	1.43 ± 0.27	19 %
Radiometric gain	0.15 ± 0.09	60 %	0.16 ± 0.09	56 %
ILS	1.39 ± 0.44	32 %	1.32 ± 0.32	24 %
Total instrument	1.40 ± 0.43	31 %	1.33 ± 0.32	24 %
Smoothing	0.15 ± 0.02	13 %	0.19 ± 0.04	21 %
Aerosol interference	0.47 ± 0.63	134 %	0.43 ± 0.47	109 %
Interference w/o aerosol	0.18 ± 0.11	61 %	0.28 ± 0.16	57 %
Variable	0.93 ± 0.59	63 %	0.94 ± 0.44	47 %
Total	2.16 ± 0.56	26 %	2.17 ± 0.42	19 %

Table 4. Global mean errors in XCO_2 and standard deviations for ocean glint observations. The coefficient of variation (relative standard deviation) is also shown.

	June		December	
Measurement	0.35 ± 0.10	29 %	0.41 ± 0.07	17 %
SCO_2 line strength	0.27 ± 0.09	33 %	0.20 ± 0.10	50 %
WCO_2 line strength	0.86 ± 0.07	8 %	0.91 ± 0.09	10 %
O_2 line strength	0.74 ± 0.05	7 %	0.72 ± 0.03	4 %
O_2 line width	0.37 ± 0.03	8 %	0.36 ± 0.02	6 %
O_2 width T dependence	0.16 ± 0.03	19 %	0.22 ± 0.08	36 %
Line mixing SCO_2	0.07 ± 0.05	71 %	0.10 ± 0.05	50 %
Line mixing O_2	0.28 ± 0.09	32 %	0.23 ± 0.08	35 %
Speed dependence WCO_2	0.31 ± 0.03	10 %	0.33 ± 0.03	9 %
Total spectroscopy	1.32 ± 0.04	3 %	1.35 ± 0.05	4 %
Radiometric gain	0.28 ± 0.10	36 %	0.27 ± 0.07	26 %
ILS	0.88 ± 0.12	14 %	0.84 ± 0.16	19 %
Total Instrument	0.93 ± 0.13	14 %	0.88 ± 0.15	17 %
Smoothing	0.15 ± 0.02	13 %	0.15 ± 0.02	13 %
Aerosol	0.37 ± 0.72*	195 %	0.19 ± 0.25	132 %
Interference w/o aerosol	0.06 ± 0.06	100 %	0.08 ± 0.05	63 %
Variable	0.62 ± 0.67*	108 %	0.52 ± 0.23	44 %
Total	1.77 ± 0.54*	31 %	1.69 ± 0.18	11 %

* driven by Sahara dust and high-latitude outliers.

The Monte Carlo approach can interrogate the probability distribution of retrieval errors under specified conditions and can characterize correlations between multiple error sources, such as interference and nonlinearity, for example. Monte Carlo studies require far more computational effort than the linear error analysis, so experiments should be designed for a carefully selected subset of conditions.

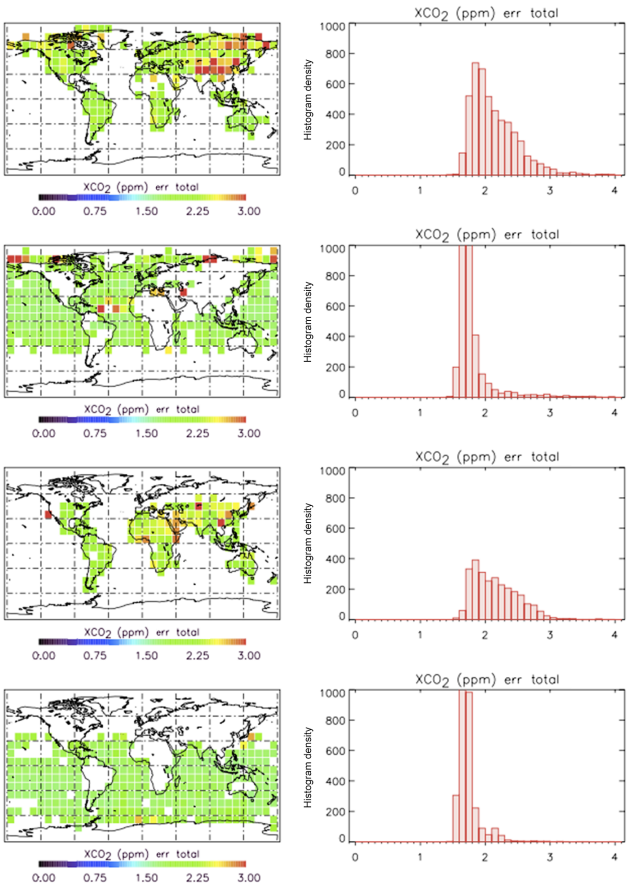

Figure 6. Total error. Top: June, land; second row: June, ocean; third row: Dec. land; bottom: Dec., ocean.

Specific recommendations for linear error analysis include the following. Linear error analysis, as applied here to simulations, will be used to estimate uncertainties in selected sets of actual OCO-2 measurements. This work will have two main goals. First, we will analyze sets of OCO-2 measurements, which have been used for top-down error estimates and validation, by comparison to data from TCCON (the Total Carbon Column Observing Network) and by examining observed scatter in uniform, local areas. The volume of OCO-2 data has provided a large collection of validation data sets for many regions, spanning all seasons. The results of these top-down estimates will be compared to the bottom-up estimates of linear error analysis. If these two types of estimates are consistent they will give us confidence in our overall understanding of measurement uncertainty. Any inconsistencies will require further investigation. One possible source of inconsistencies, already under investigation as described above, is nonlinearity of the forward model.

Second, the variability of the bottom-up estimates will be systematically compared to the variation in sounding geometry, atmospheric conditions, and surface type. This will improve insight into the causes of measurement uncertainty, and guide data users in quantitative applications.

7 Data availability

The simulations and analyses reported in this paper are not a part of the OCO-2 data set or of the public record of the OCO-2 project. They are exploratory in nature and not publically accessible because it has not been feasible to select, catalog, and document the relevant material.

The Supplement related to this article is available online at doi:10.5194/amt-9-5227-2016-supplement.

Acknowledgements. We thank the following members of the OCO-2 team for support and helpful discussions: Vijay Natraj, Linda Brown, Brian Drouin, Chris Benner, Malathy Devi, and Annmarie Eldering. Part of the research was carried out at the Jet Propulsion Laboratory, California Institute of Technology, under a contract with the National Aeronautics and Space Administration. The CSU contribution to this work was supported by JPL subcontract 1439002. The contribution by BC Scientific Consulting was supported by JPL subcontract 1518224.

Edited by: I. Aben
Reviewed by: two anonymous referees

References

Benner, D. C., Devi, V. M., Nugent, E., Sung, K., Brown, L. R., Miller C. E., and Toth, R. A.: Line parameters of carbon dioxide in the 4850 cm^{-1} region, Twenty-second Coll. on High Res. Mol. Spectrosc., Dijon, France, poster N19, 2011.

Bösch, H., Baker, D., Connor, B., Crisp, D., and Miller, C.: Global Characterization of CO_2 Column Retrievals from Shortwave-Infrared Satellite Observations of the Orbiting Carbon Observatory-2 Mission, Remote Sens., 3, 270–304, 2011.

Brown, L. R. and Plymate, C.: Experimental Line Parameters of the Oxygen A Band at 760 nm, J. Mol. Spectrosc. 199, 166–179, 2000.

Buchard, V., da Silva, A. M., Colarco, P. R., Darmenov, A., Randles, C. A., Govindaraju, R., Torres, O., Campbell, J., and Spurr, R.: Using the OMI aerosol index and absorption aerosol optical depth to evaluate the NASA MERRA Aerosol Reanalysis, Atmos. Chem. Phys., 15, 5743–5760, doi:10.5194/acp-15-5743-2015, 2015.

Butz, A., Hasekamp, O. P., Frankenberg, C., and Aben, I.: Retrievals of atmospheric CO_2 from simulated space-borne measurements of backscattered near-infrared sunlight: accounting for aerosol effects, Appl. Optics, 48, 3322–3336, 2009.

Connor, B. J., Bösch, H., Toon, G., Sen, B., Miller, C., and Crisp, D.: Orbiting Carbon Observatory: Inverse method and prospective error analysis, J. Geophys. Res., 113, D05305, doi:10.1029/2006JD008336, 2008.

Crisp, D., Miller, C., and DeCola, P.: NASA Orbiting Carbon Observatory; measuring the column averaged carbon dioxide mole fraction from space, J. Appl. Remote Sens., 2, 023508, doi:10.1117/1.2898457, 2008.

Devi, V. M., Benner, D. C., Brown, L. R., Miller, C. E., and Toth, R. A.: Line mixing and speed dependence in CO_2 at 6227.9 cm^{-1}: Constrained multispectrum analysis of intensities and line shapes in the 30013 ← 00001 band, J. Mol. Spectrosc. 245, 52–80, 2007.

Devi, V. M., Benner, D. C., Sung, K., Brown, L. R., Crawford, T. J., Miller, C. E., Drouin, B. J., Payne, V. H., Yu, S., Smith, M. A. H., Mantz, A. M., and Gamache, R. R.: Line parameters including temperature dependences of self- and air-broadened line shapes of $^{12}C^{16}O_2$: 1.6-μm region, J. Quant. Spectrosc. and Ra., 177, 117–144, 2016.

Drouin, B. J., Benner, D. C., Brown, L. R., Cich, M. J., Crawford, T. J., Devi, V. M., Guillaume, A., Hodges, J. T., Mlawer, E. J., Robichaud, D. J., Oyafuso, F., Payne, V. H., Sung, K., Wishnow, E. H., and Yu, S.: Multispectrum analysis of the oxygen A-band, J. Quant. Spectrosc. Ra., in press, 2016.

Joly, L., Marnas, F., Gibert, F., Bruneau, D., Grouiz, B., Flamant, P. H., Durry, G., Dumelie, N., Parvitte, B., and Zeninari, V.: Laser diode absorption spectroscopy for accurate CO_2 line parameters at 2 microns: consequences for space-based DIAL measurements and potential biases, Appl. Optics, 48, 5475–5483, 2009.

JPL: OCO-2 Level 2 Full Physics Retrieval Algorithm Theoretical Basis, Version 2.0 Rev 2, available at: http://disc.sci.gsfc.nasa.gov/OCO-2/documentation/oco-2-v6/OCO2_L2_ATBD.V6.pdf, 2015.

Jung, Y., Kim, J., Kim, W. Boesch, H., Lee, H., Cho, C., and Tae-Young, G.: Impact of Aerosol Property on the Accuracy of a CO_2 Retrieval Algorithm from Satellite Remote Sensing, Remote Sens., 8, 322, doi:10.3390/rs8040322, 2016.

Lee, R. A. M., O'Dell, C. W., Wunch, D., Roehl, C. M., Osterman, G. B., Blavier, J.-F., Rosenberg, R., Chapsky, L., Frankenberg, C., Hunyadi-Lay, S. L., Fisher, B. M., Rider, D. M., Crisp, D., and Pollock, R.: Preflight Spectral Calibration of the Orbiting Carbon Observatory, IEEE T. Geosci. Remote, submitted, 2016.

Long, D. A., Havey, D. K., Okumura, M., Miller, C. E., and Hodges, J. T.: O_2 A-band line parameters to support atmospheric remote sensing, J. Quant. Spectrosc. Ra., 111, 2021–2036, doi:10.1016/j.jqsrt.2010.05.011, 2010.

Long, D. A., Robichaud, D. J., and Hodges, J. T.: Frequency-stabilized cavity ring-down spectroscopy measurements of line mixing and collision-induced absorption in the O_2 A-band, J. Chem. Phys. 137, 014307; doi:10.1063/1.4731290, 2012.

O'Brien, D. M., Polonsky, I., O'Dell, C., and Carheden, A.: Orbiting Carbon Observatory (OCO), Algorithm Theoretical Basis Document, the OCO simulator, Technical Report ISSN 0737-5352-85, Cooperative Institute for Research in the Atmosphere, Colorado State University, Fort Collins, CO, USA, 2009.

O'Dell, C. W., Connor, B., Bösch, H., O'Brien, D., Frankenberg, C., Castano, R., Christi, M., Eldering, D., Fisher, B., Gunson, M., McDuffie, J., Miller, C. E., Natraj, V., Oyafuso, F., Polonsky, I., Smyth, M., Taylor, T., Toon, G. C., Wennberg, P. O., and Wunch, D.: The ACOS CO_2 retrieval algorithm – Part 1: Description and validation against synthetic observations, Atmos. Meas. Tech., 5, 99–121, doi:10.5194/amt-5-99-2012, 2012.

Polyansky, O. L., Bielska, K., Ghysels, M., Lodi, L., Zobov, N. F., Hodges, J. T., and Tennyson, J.: High-accuracy CO_2 line intensities determined from theory and experiment, Phys. Rev. Lett., 114, 243001, doi:10.1103/PhysRevLett.114.243001, 2015.

Rienecker, M. M., Suarez, M. J., Gelaro, R., Todling, R., Bacmeister, J., Liu, E., Bosilovich, M. G., Schubert, S. D., Takacs, L., Kim, G.-K., Bloom, S., Chen, J., Collins, D., Conaty, A., da Silva, A., Gu, W., Joiner, J., Koster, R. D., Lucchesi, R., Molod, A., Owens, T., Pawson, S., Pegion, P., Redder, C. R., Reichle, R., Robertson, F. R., Ruddick, A. G., Sienkiewicz, M., and Woollen, J., MERRA: NASA's Modern-Era Retrospective Analysis for Research and Applications, J. Climate, 24, 3624–3648, 2011.

Robichaud, D. J., Hodges, J. T., Brown, L. R., Lisak, D., Maslowski, P., Yeung, L. Y., Okumura, M., and Miller, C. E.: Experimental intensity and line shape parameters of the oxygen A-band using frequency-stabilized cavity ring-down spectroscopy, J. Mol. Spectrosc., 248, 1–13, 2008.

Rodgers C. D.: Inverse Methods for Atmospheric Sounding, World Scientific, Singapore, 2000.

Rodgers, C. D. and Connor, B. J.: Intercomparison of remote sounding instruments, J. Geophys. Res. 108, 4116, doi:10.1029/2002JD002299, 2003.

Rosenberg, R., Maxwell, S., Johnson B. C., Chapsky, L., Lee, R. A. M., and Pollock, R.: Preflight Radiometric Calibration of Orbiting Carbon Observatory, IEEE T. Geosci. Remote, 2, in press, 2016.

Sung, K., Brown, L. R., Toth, R. A., and Crawford, T. J.: Fourier transform infrared spectroscopy measurements of H_20-broadened half-widths of CO_2 at 4.3 um, Can. J. Phys., 87, 469–484, 2009.

Taylor, T. E., O'Dell, C. W., Frankenberg, C., Partain, P. T., Cronk, H. Q., Savtchenko, A., Nelson, R. R., Rosenthal, E. J., Chang, A. Y., Fisher, B., Osterman, G. B., Pollock, R. H., Crisp, D., Eldering, A., and Gunson, M. R.: Orbiting Carbon Observatory-2 (OCO-2) cloud screening algorithms: validation against collocated MODIS and CALIOP data, Atmos. Meas. Tech., 9, 973–989, doi:10.5194/amt-9-973-2016, 2016.

Wunch, D., Wennberg, P. O., Toon, G. C., Connor, B. J., Fisher, B., Osterman, G. B., Frankenberg, C., Mandrake, L., O'Dell, C., Ahonen, P., Biraud, S. C., Castano, R., Cressie, N., Crisp, D., Deutscher, N. M., Eldering, A., Fisher, M. L., Griffith, D. W. T., Gunson, M., Heikkinen, P., Keppel-Aleks, G., Kyrö, E., Lindenmaier, R., Macatangay, R., Mendonca, J., Messerschmidt, J., Miller, C. E., Morino, I., Notholt, J., Oyafuso, F. A., Rettinger, M., Robinson, J., Roehl, C. M., Salawitch, R. J., Sherlock, V., Strong, K., Sussmann, R., Tanaka, T., Thompson, D. R., Uchino, O., Warneke, T., and Wofsy, S. C.: A method for evaluating bias in global measurements of CO_2 total columns from space, Atmos. Chem. Phys., 11, 12317–12337, doi:10.5194/acp-11-12317-2011, 2011.

Yoshida, Y., Ota, Y., Eguchi, N., Kikuchi, N., Nobuta, K., Tran, H., Morino, I., and Yokota, T.: Retrieval algorithm for CO_2 and CH_4 column abundances from short-wavelength infrared spectral observations by the Greenhouse gases observing satellite, Atmos. Meas. Tech., 4, 717–734, doi:10.5194/amt-4-717-2011, 2011.